Material Model Evaluation of a Composite Honeycomb Energy Absorber

Karen E. Jackson
NASA Langley Research Center
Hampton, VA

Edwin L. Fasanella
National Institute of Aerospace
Hampton, VA

Martin S. Annett
NASA Langley Research Center
Hampton, VA

Michael A. Polanco
ATK Space Systems
Hampton, VA

Abstract

A study was conducted to evaluate four different material models in predicting the dynamic crushing response of solid-element-based models of a composite honeycomb energy absorber, designated the Deployable Energy Absorber (DEA). Dynamic crush tests of three DEA components were simulated using the nonlinear, explicit transient dynamic code, LS-DYNA®. In addition, a full-scale crash test of an MD-500 helicopter, retrofitted with DEA blocks, was simulated. The four material models used to represent the DEA included: *MAT_CRUSHABLE_FOAM (Mat 63), *MAT_HONEYCOMB (Mat 26), *MAT_SIMPLIFIED_RUBBER/FOAM (Mat 181), and *MAT_TRANSVERSELY_ANISOTROPIC_CRUSHABLE_FOAM (Mat 142). Test-analysis calibration metrics included simple percentage error comparisons of initial peak acceleration, sustained crush stress, and peak compaction acceleration of the DEA components. In addition, the Roadside Safety Verification and Validation Program (RSVVP) was used to assess similarities and differences between the experimental and analytical curves for the full-scale crash test.

Introduction

Since 2006, NASA has sponsored research to evaluate a composite honeycomb energy-absorbing concept, designated the Deployable Energy Absorber (DEA) [1]. The DEA is an expandable composite honeycomb structure designed to absorb impact energy by crushing, which is achieved through local cell wall bending, plastic hinge formation, minor tearing, and delamination. Unlike other cellular energy absorbers in use today, the DEA utilizes a unique and patented flexible hinge at each junction of its cell walls [2]. This feature allows the energy absorber to be stowed flat until needed for deployment during an emergency. Expansion can be performed in a linear or rotational manner, as shown in Figure 1. Like conventional honeycomb, once expanded the energy absorber is transformed into an efficient orthotropic cellular structure, with greater stiffness and strength along the cell axis as compared to the transverse directions.

Experimental evaluation of the DEA utilized a building block approach that included material characterization testing of its constituent, Kevlar®-129 fabric/epoxy; flexural testing of single hexagonal cells; dynamic crush tests of multi-cell components; and vertical drop tests of a composite fuselage section, retrofitted with DEA blocks, onto concrete, water, and soft soil [3-5]. As a final demonstration, a full-scale crash test of an MD-500 helicopter was conducted in December 2009 to assess the energy absorbing capabilities of the DEA under combined velocity impact conditions, and to generate data for model validation [6-8]. During each stage of the DEA evaluation process, finite element models of the test articles were developed and

simulations were performed using the explicit, nonlinear transient dynamic finite element code, LS-DYNA® [9].

(a) Linear deployment.   (b) Radial deployment.
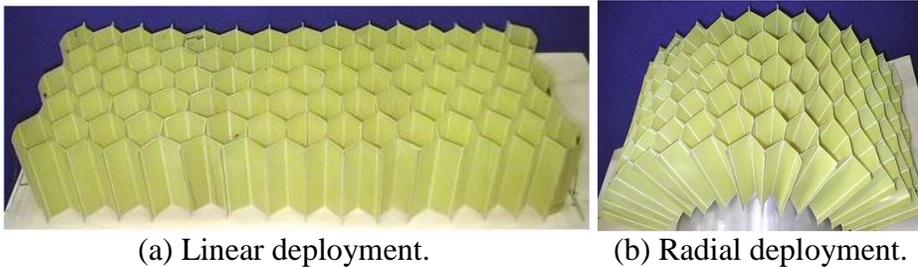
Figure 1. Photographs showing deployment methods of the DEA.

As part of the simulation studies, both shell- and solid-element based models were developed. Shell element models contained accurate physical representations of the DEA cellular geometry and these models were able to successfully predict the observed deformation modes and the crushing responses of the DEA [10-13]. However, in order to capture these responses, a fairly fine mesh was required, typically with a nominal element edge length of 0.25-in. As a result, simulations of tests involving large DEA blocks required tens of thousands of shell elements to adequately represent the DEA. Under dynamic compressive loading, these elements can experience severe deformations, leading to small time steps and long execution times.

As an alternative, solid-element-based models of the DEA were investigated [14-16]. A major challenge of this approach was to find an appropriate material model that could accurately capture the major features of the DEA crushing response, including initial peak acceleration, uniform sustained crushing, and compaction. In this paper, four different material models (Mat 63, Mat 26, Mat 181, and Mat 142) were evaluated in solid-element models of three DEA components. In addition, the same material definitions were used in solid-element-based representations of DEA blocks attached to the MD-500 helicopter, and full-scale crash simulations were executed. For the DEA components, test-analysis calibration metrics included simple percentage error comparisons of initial peak acceleration, sustained crush stress, and peak compaction acceleration. For the MD-500 crash test, the Roadside Safety Verification and Validation Program (RSVVP) [17] was used to assess similarities and differences between the experimental and analytical acceleration time histories for the full-scale crash test.

Summary of Experiments

Dynamic Crush Tests of Three DEA Components
Three multi-cell components were fabricated to evaluate the energy absorption capabilities of the DEA under both normal and off-axis loading conditions. Two of the DEA components, consisting of 59- and 104-cells, were manufactured such that the longitudinal axes of the cells were oriented in the same direction as loading (normal). A third DEA component, consisting of 68-cells, was fabricated such that the longitudinal axes of the cells were canted by 27° with respect to the direction of loading (off-axis). Each component was fabricated of Kevlar®-129 fabric/epoxy with fibers oriented at ±45° with respect to the longitudinal or loading axis. Individual cells within the honeycomb have a hexagonal cross-section with a flat facet width of 1-in. and a nominal wall thickness of 0.01-in. This particular configuration of the DEA was designed to provide a 20-psi uniform crushing stress. The top surface of each DEA component

was curved slightly to reduce the high peak loads that can occur during initial impact. The components were impacted in a fully deployed state by a rigid impact mass, or block, that translated on vertical support rods through low-friction bearings. The drop mass was instrumented with an accelerometer to record the vertical acceleration response of the impact block. Details regarding the dimensions of each DEA component and the impact test conditions are listed in Table 1.

Table 1. Details of DEA Component Crush Testing.

Number of cells	Cell orientation*	Length, in.	Width, in.	Height, in.	Weight of impact block, lb.	Velocity at impact, in/s
59	0°	16	12.4	6.0	412.5	195.6
104	0°	21	15.8	10.0	477.2	266.4
68	27°	16	14.0	6.7	477.2	183.6

*with respect to the vertical, or loading, direction

Plots of raw and filtered acceleration time histories for each DEA component are shown in Figure 2. The test data were filtered using either an SAE CFC 60 or 180 low pass filter [18], as necessary to remove high frequency oscillations from the data. All three DEA components exhibit a uniform crushing phase; however, only the 59- and 68-cell components exhibit a compaction phase, which is characterized by a large increase in acceleration near the end of the pulse due to "bottoming out" of the honeycomb. The 104-cell component did not achieve compaction, even though a higher impact mass and velocity were used during the impact test. Obviously, the incident kinetic energy was insufficient to produce compaction due to the greater cross-sectional area and height of the 104-cell DEA. It should be noted that no repeated tests of similar components were performed to quantify experimental uncertainty.

(a) 59-cell DEA.   (b) 104-cell DEA.   (c) 68-cell DEA.
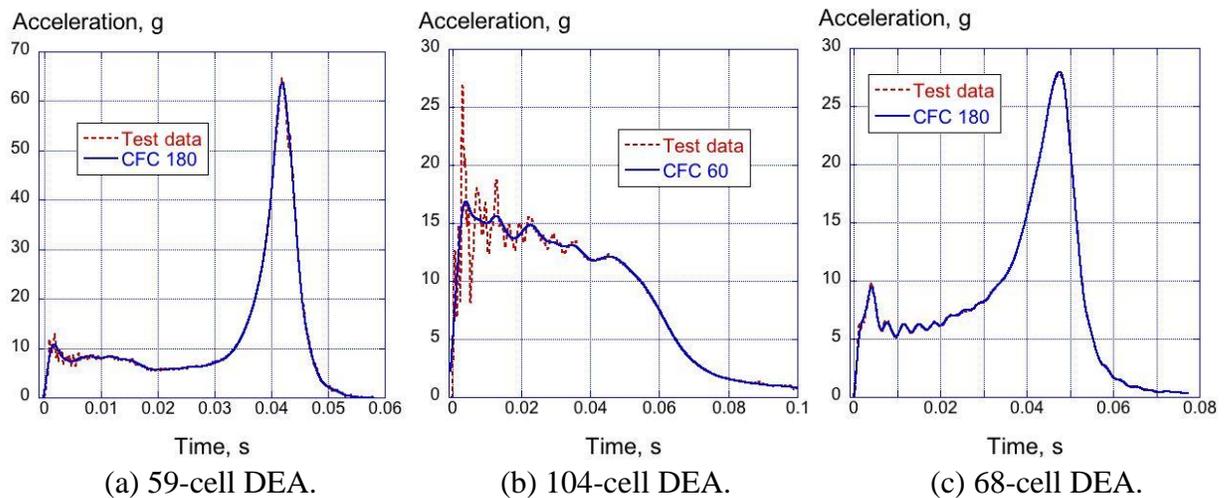
Figure 2. Raw and filtered acceleration responses from three DEA component crush tests.

All of the material definitions that were selected for evaluation in solid-element-based models of the DEA require input of curves that define the stress versus volumetric strain response of the material. To generate these curves, the filtered acceleration time histories, shown in Figure 2, were converted to stress-strain data, using the following procedure. Stress values were calculated by adding 1 to the acceleration data in g's to account for the acceleration of gravity, then multiplying by the weight of the impact block, and dividing by the cross-sectional area of

the DEA. The strain was determined by double integration of the acceleration response to obtain displacement, which was divided by the initial vertical height of the DEA component. The average crush stress of the 59-, 104-, and 68-cell DEA components was determined based on a strain interval of 0- to 0.6-in/in. The average stress values are 15.6-psi for the 68-cell DEA, 17.6-psi for the 59-cell DEA, and 22.0-psi for the 104-cell DEA. If the crush stresses of the two normal DEA components (59- and 104-cell) are averaged, a value of 19.8-psi is obtained, which is close to the design goal of 20-psi. Please note that values of average crush stress reported later are based on converting average accelerations determined over the time interval of 0.0-0.03-s. These numbers may differ slightly based on the different intervals used in the calculations.

A plot of the 59- and 104-cell DEA stress versus volumetric strain responses is shown in Figure 3, along with a curve that was obtained by averaging the 59- and 104-cell responses. Since the 104-cell DEA did not reach the compaction phase during the test, its stress-strain curve was approximated to have the same response as the 59-cell DEA after a strain of approximately 0.8-in/in. In this paper, the average stress-strain response was used as input to the material models. Stress values up to 30-psi are shown in the plot; however, the actual curve has a high magnitude "tail" that is not shown in Figure 3 which is used to simulate compaction and to prevent element inversion and negative volume erros.
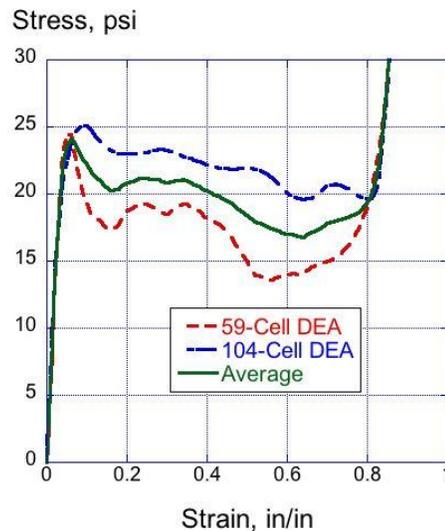
Figure 3. Stress-strain responses of the 59- and 104-cell DEA, and the 59- and 104-cell average.

Full-Scale Crash Test of an MD-500 Helicopter
An impact simulation was performed representing a full-scale crash test of an MD-500 helicopter, retrofitted with two blocks of the DEA. The test was conducted onto a flat concrete surface. Pre- and post-test photographs of the test article are shown in Figure 4. The crash test was conducted at the NASA Langley Landing and Impact Research (LandIR) Facility in December 2009 to evaluate the performance of the DEA under realistic crash conditions and to generate test data for comparison with finite element predictions. The pilot was a 50th percentile male Hybrid III Anthropomorphic Test Device (ATD). The co-pilot and one passenger were 50th percentile male Hybrid II ATDs. The other passenger was a biofidelic torso developed by The Johns Hopkins University Applied Physics Laboratory [19]. ATDs were seated in standard military replacement seats that were installed in the helicopter. The total weight of the test article was 2,930 lb, including four ATDs, two DEA blocks, and ballast mass that was added to represent the main rotor, engine, tail, and fuel tank. The helicopter was instrumented to collect

160 channels of data from strain gages, accelerometers, and load cells at 10,000 samples/second. In addition, photogrammetric targets were placed on the left side of the vehicle. Motion tracking of the targets was used to determine impact conditions and gross vehicle motion before, during, and after impact.

The DEA blocks attached to the MD-500 helicopter had a design configuration similar to the three DEA components. A prior analytical study [12] showed that the ideal orientation of the DEA blocks for maximum energy absorption given the combined velocity conditions of the full-scale crash test was a 20° cant angle with respect to the vertical direction. However, geometric limitations of the airframe required that the orientation of the rear DEA block remain purely vertical. Consequently, only the front DEA block was canted by 20°. The DEA blocks were attached in their fully deployed configuration. Measured impact conditions were 25.6-ft/s horizontal and 38.8-ft/s vertical velocities with an attitude of 5.7° pitch, 9.3° yaw, and 7.0° roll. For the present simulation study, test-analysis comparisons are shown for two locations, one at the pilot seat box and the other at a passenger floor location near the rear bulkhead. Additional details of the experimental program can be found in References 6-8.

| (a) Pre-test photograph. | (b) Post-test photograph. |

Figure 4. Pre- and post-test photographs of the MD-500 test article.

Descriptions of the Material Models

Solid-element-based finite element models of the dynamic crush tests of the DEA components were developed for execution in LS-DYNA$^®$ Shared Memory Processor (SMP) version 971. Initially, solid elements were selected for the simulations as a means of lowering execution times, compared with shell-element-based simulations. However, it was also understood that the use of solid-element-based models precluded the accurate prediction of deformation modes observed in the actual DEA specimens. The objective of this simulation study was to evaluate four different material models assigned to solid-element-based models of the DEA and to determine if these models could adequately predict both the uniform crush and compaction responses of the normal and off-axis DEA components. Four different material property definitions available in LS-DYNA$^®$ were evaluated, including: Mat 63 (*MAT_CRUSHABLE_FOAM), Mat 26 (*MAT_HONEYCOMB), Mat 181 (*MAT_SIMPLIFIED_RUBBER/FOAM), and Mat 142 (*MAT_TRANSVERSELY_ANISO-TROPIC_CRUSHABLE_FOAM). In addition, the finite element model of the MD-500 was updated with solid element representations of the DEA blocks, and the full-scale crash test was

simulated in which these four material models were assigned to the energy absorbers. In the following subsections of the paper, each of the material models will be described briefly.

Mat 63 (*MAT_CRUSHABLE_FOAM)
This material model was developed to represent the properties of isotropic crushable foam and includes optional damping and a tensile cutoff stress. Unloading is fully elastic to the tensile cutoff stress and reloading follows the loading curve. Tension is represented using an elastic-perfectly-plastic response at the tension cutoff value [9]. Mat 63 allows input of a user-defined curve representing the yield stress versus volumetric strain response of the material. It is important to note that volumetric strain is defined as 1 minus the relative volume, which is the ratio of the current volume to the initial volume. Thus, as crushing starts, the volumetric strain is low and increases as crushing progresses. The input values used in the Mat 63 material model are listed in Table 2. The input stress-strain curve for Mat 63 was the average response shown in Figure 3. The value of Young's modulus, shown in Table 2, was determined from the high-magnitude tail of the average stress-strain curve, not the initial stress-strain response. LS-DYNA® uses the high value to prevent instabilities in the model.

Table 2. Mat 63 input parameters.

Parameter	Description	Value
RO	Material density	2.182e-6 lb-s^2/in^4
E	Young's modulus	6000 psi
PR	Poisson's ratio	0.05
LCID	Identification number of user input stress-strain response	Average response
TSC	Tensile stress cutoff	-5 psi
DAMP	Damping coefficient	0.05

Mat 26 Honeycomb Material Model
The Mat 26 material model is used to represent honeycomb and foam materials with anisotropic behavior [9]. Nonlinear elastic-plastic material responses are defined separately for normal and shear stresses, and these input curves are considered to be fully uncoupled. The behavior of the material before compaction is orthotropic, where the components in the stress tensor are uncoupled. Unloading is based on the interpolated Young's modulus, which must provide an unloading tangent that exceeds the loading tangent. The input values used in the Mat 26 material model for both the normal and off-axis DEA components are listed in Table 3.

In this study, the input stress-strain curves are based on volumetric strain. The user of this material model is cautioned in Reference 9 to ensure that each input curve contains the exact same number of points and this recommendation was followed. The input load curve for Mat 26, shown in Figure 5, was based on the average stress-strain response. Unlike the input curve for Mat 63 which begins at zero stress and zero strain, the Mat 26 input curve begins with a point having negative strain and positive stress and the second point has a corresponding value of positive strain and the same value of positive stress. This approach for inputting the load curves for Mat 26 is recommended in Reference 9.

The Mat 26 input curve, shown in Figure 5, corresponds to the load curve for sigma-cc (LCC listed in Table 3), where cc was arbitrarily selected to represent the local vertical direction.

Since no experimental data were available, load curve inputs for the two transverse directions (aa and bb) and for the shear directions (s, ab, bc, ca) were assumed to be scaled versions of sigma-cc (LCC), with the scale factors listed in Table 3. Finally, Mat 26 allows the user to define directions for the local material axis system using the AOPT parameter [9]. For these simulations, AOPT was set to 2.0 indicating globally orthotropic behavior with material axes determined by vectors **a** and **d**, such that **a** x **d** defines the primary material direction. Note that the local material axes can rotate based on element deformation and nodal angular velocity. For the 59- and 104-cell DEA components, the vectors were chosen such that the primary material direction (cc) is oriented vertically, as illustrated in Figure 6(a). For the 68-cell DEA, the vectors were defined such that the primary material axis for LCC was canted 27° with respect to the vertical direction, as illustrated in Figure 6(b).

Table 3. Mat 26 input parameters.

Symbol	Description	Value	
		Normal DEA	**Off-axis DEA**
RO	Material density, lb-s^2/in^4	2.182e-6	2.182e-6
E	Young's modulus of fully compacted honeycomb, psi	6,000.0	6,000.0
PR	Poisson's ratio	0.05	0.05
SIGY	Yield stress of fully compacted honeycomb, psi	22.0	22.0
VF	Relative volume at which honeycomb is fully compacted	0.15	0.15
MU	Damping coefficient	0.05	0.05
BULK	Bulk viscosity flag, if equal 0.0, bulk viscosity is not used	0.0	0.0
LCA	Load curve id for stress sigma-aa versus volumetric strain	SF*=0.1	SF*=0.1
LCB	Load curve id for stress sigma-bb versus volumetric strain	SF=0.1	SF=0.1
LCC	Load curve id for stress sigma-cc versus volumetric strain	SF=1.0	SF=1.0
LCS	Load curve id for shear stress versus volumetric strain	No input	No input
LCAB	Load curve id for stress sigma-ab versus volumetric strain	SF=0.45	SF=0.45
LCBC	Load curve id for stress sigma-bc versus volumetric strain	SF=0.45	SF=0.45
LCCA	Load curve id for stress sigma-ca versus volumetric strain	SF=0.45	SF=0.45
LCSR	Load curve id for strain rate effects (optional)	No input	No input
EAAU	Elastic modulus Eaau in uncompressed configuration, psi	60.0	60.0
EBBU	Elastic modulus Ebbu in uncompressed configuration, psi	60.0	60.0
ECCU	Elastic modulus Eccu in uncompressed configuration, psi	566.7	566.7
GABU	Shear modulus Gabu in uncompressed configuration, psi	135.0	135.0
GBCU	Shear modulus Gbcu in uncompressed configuration, psi	270.0	270.0
GCAU	Shear modulus Gcau in uncompressed configuration, psi	270.0	270.0
AOPT	Material axes option (equal 2.0 – globally orthotropic)	2.0	2.0
MACF	Material axis change flag (default=1, no change)	1.0	1.0
XP YP ZP	Coordinates of point p for AOPT = 1	No input	No input
A1 A2 A3	Coordinates of vector **a** for AOPT = 2	1, 0, 0	.891, 0, -.454
D1 D2 D3	Coordinates of vector **d** for AOPT = 2	0, 1, 0	0, 1, 0
TSEF	Tensile strain at element failure (element will erode)	No input	No input
SSEF	Shear strain at element failure (element will erode)	No input	No input

*SF is a Scale Factor applied to the primary input load curve (LCC)

Mat 181 *MAT_SIMPLIFIED_RUBBER/FOAM
As described in Reference 9, Mat 181 was developed for rubber and foam materials whose assumed isotropic response can be characterized by a single uniaxial load curve. The material

can be used with both shell and solid elements and has strain rate capability. Parameter values for Mat 181 representing the DEA material response are listed in Table 4. The input load curve, which is based on the average test data, is shown in Figure 7(a) and a closer view of the plot is shown in Figure 7(b) for a much narrower ordinate range. These plots show that the data are input in the negative stress, negative strain quadrant.

Figure 5. Mat 26 input load curve based on the averaged 59- and 104-cell DEA data.

(a) Normal DEA.   (b) Off-axis DEA.
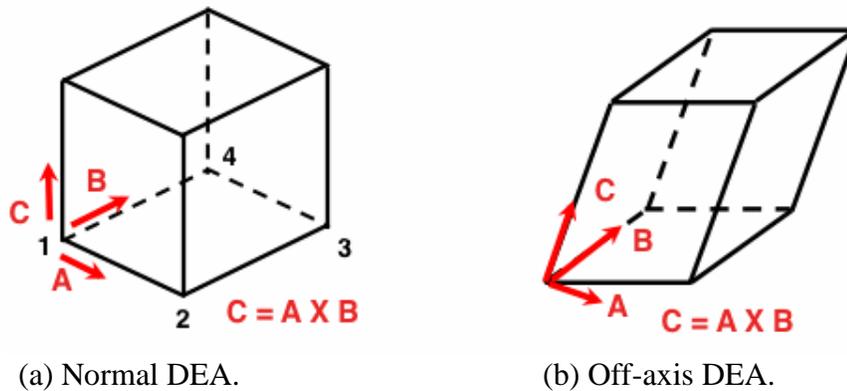
Figure 6. Schematics illustrating local material axis definitions for normal and off-axis DEA components.

Mat 142 *MAT_TRANSVERSELY_ANISOTROPIC_CRUSHABLE_FOAM

Mat 142 was developed for extruded low-density crushable foams that exhibit anisotropic behavior with zero Poisson's Ratio. The formulation of this material model is described in Reference 20, and it was developed to correct some problems seen in Mat 26 in representing off-axis loading. Specifically, this material model requires input of load curves to represent the nominal axial stress versus volumetric strain (I11), as well as three additional load curves representing nominal transverse stress, shear stress in the 1-2 direction, and shear stress in the 2-3 direction. It is important to note that curve I11 is aligned with the element local material direction, A. As an option, the user can define a stress versus volumetric strain response for load

at a specified off-axis angle. Input values for Mat 142 representing the DEA material response are listed in Table 5.

Table 4. Mat 181 input parameters.

Symbol	Description	Value
RO	Material density, lb-s^2/in^4	2.182e-6
KM	Linear bulk modulus	2222.2
MU	Damping coefficient	0.2
G	Shear modulus for frequency independent damping	No input
SIGF	Limit stress for frequency independent damping	No input
REF	Reference geometry flag	No input
PRTEN	Tensile Poisson's ratio for shells	No input
SGL	Specimen gage length	1.0
SW	Specimen width	1.0
ST	Specimen thickness	1.0
LC/TBID	Load curve or table ID	Average
TENSION	Parameter that controls how rate effects are managed	No input
RTYPE	Strain rate type	1.0
AVGOPT	Averaging option	1.0
PR/BETA	If between 0<PR<0.5, Poisson's ratio	0.05
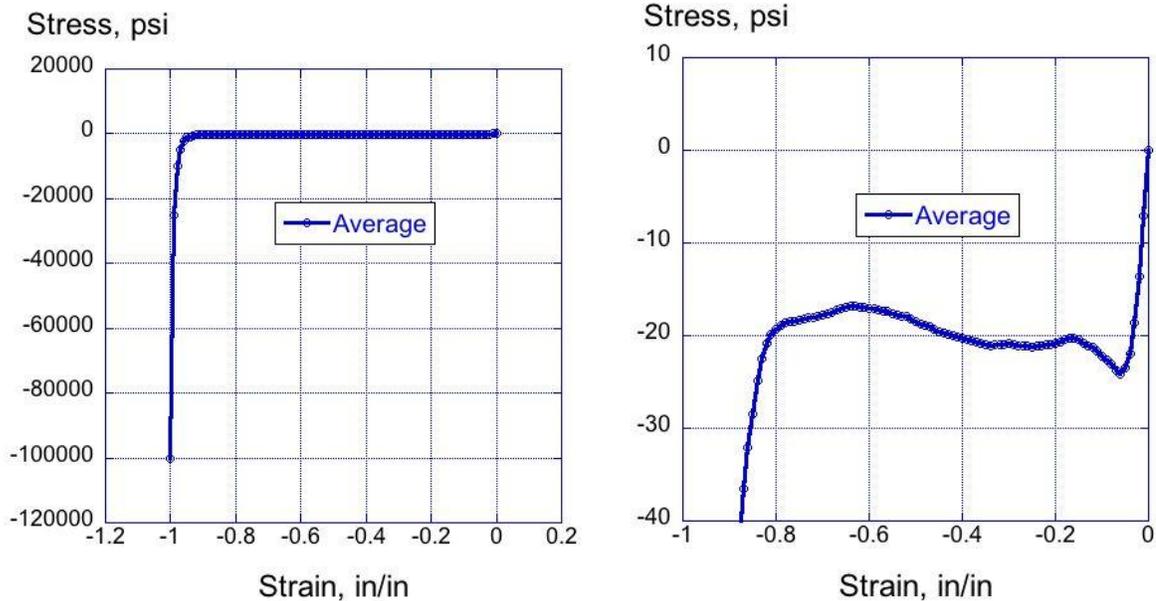
(a) Load curve input to Mat 181.   (b) Load curve input, narrowed ordinate range.

Figure 7. Input load curve (stress versus strain) for Mat 181, based on the average response.

Note that in Table 5 the input load curves in the transverse and shear directions are simply scaled versions of the nominal axial load curve (I11), and the scale factors are the same as used in Mat 26. Also, during an early evaluation of this material, the optional load curve, IAA, was input based on the stress versus volumetric strain response of the 68-cell DEA and ANG was set to 27°. However, the simulations developed extremely small time steps and negative volume errors occurred. Consequently, load curve IAA was removed. Finally, the same input load curve used for Mat 26 was used for Mat 142, as shown in Figure 5.

Table 5. Mat 142 input parameters.

Symbol	Description	Value Normal DEA	Value Off-Axis DEA
RO	Material density, lb-s^2/in^4	2.182e-6	2.182e-6
E11	Elastic modulus in the axial direction	712.0	712.0
E22	Elastic modulus in the transverse direction	71.2	71.2
E12	Elastic shear modulus	270.0	270.0
E23	Elastic shear modulus in the transverse plane	135.0	135.0
G	Shear modulus	339.0	339.0
K	Bulk modulus for contact stiffness	10.0e03	10.0e03
I11	Load curve ID for axial stress vs volumetric strain	SF=1.0	SF=1.0
I22	Load curve ID for transverse stress vs volumetric strain	SF=0.1	SF=0.1
I12	Load curve ID for shear stress 12 vs volumetric strain	SF=0.45	SF=0.45
I23	Load curve ID for shear stress 23 vs volumetric strain	SF=0.45	SF=0.45
IAA	Load curve ID for stress vs. volumetric strain at angle	No input	No input
NY	Set to unity for a symmetric yield surface	1.0	1.0
ANG	Angle corresponding to load curve ID, IAA	No input	No input
MU	Damping coefficient	0.05	0.05
AOPT	Material axes option (equal 2.0 – globally orthotropic)	2.0	2.0
ISCL	Load curve ID for strain rate scale factor	No input	No input
MACF	Material axis change flag	1.0	1.0
A1, A2, A3	Coordinates of vector **a** for AOPT=2.0	0, 0, 1	0.454, 0, 0.891
D1, D2, D3	Coordinates of vector **d** for AOPT=2.0	1, 0, 0	0, 1, 0

*SF is a Scale Factor applied to the primary input load curve (I11)

Finite Element Model Descriptions

DEA Component Model Description

The 59-, 104-, and 68-cell DEA component models are shown in Figure 8. Each model consists of three main parts: the DEA, which is represented using hexagonal solid elements with element formulation 1 (default constant stress solid element); an impact surface, located just beneath the bottom surface of the DEA, that is constructed of quadrilateral shell elements; and, a rigid block that is constructed of solid hexagonal elements that are assigned a *MAT_RIGID material property. Each DEA model had a nominal element edge length of 0.5-in., which was determined based on a prior mesh discretization study. The impact surface was included to prevent element deformation below the bottom surface of the DEA. All edge nodes on the impact surface were fully constrained. The same *MAT_RIGID material property used for the impact block was assigned to the impact surface. The density of the rigid material was chosen such that the weight of each rigid block matched the test conditions, which are listed in Table 1. Likewise, nodal velocities were assigned to the block to match the test conditions. For all models, a segment-based contact definition of *CONTACT_AUTOMATIC_SINGLE_SURFACE was used to represent contact between the impact block and the DEA, the DEA and the impact surface, and self-contact between elements within the DEA. Finally, the DEA component simulations were executed to include gravity as a body load. Additional details regarding the DEA component models may be found in Reference 5.

| (a) 59-cell model. | (b) 104-cell model. | (c) 68-cell model. |
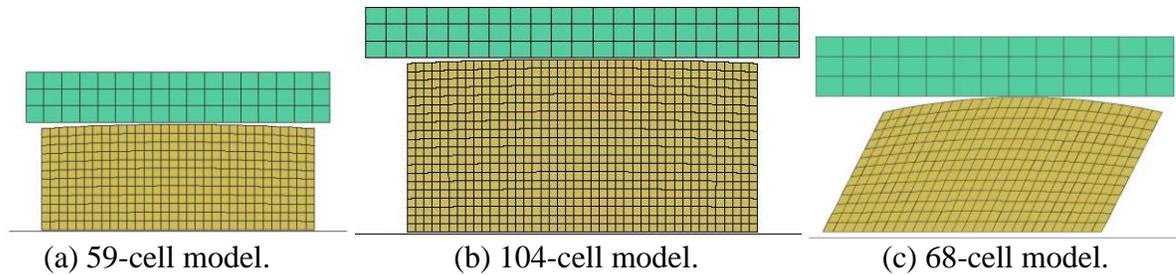
Figure 8. Solid element models of three DEA components.

MD-500 Helicopter Model

A system-integrated finite element model (FEM) of the MD-500 helicopter, shown in Figure 9, was initially developed based on a computer aided design (CAD) model of the MD-500 fuselage. The model is designated "system-integrated" because it contains accurate physical representations of the impact surface, skid gear, airframe, seats, ballast, and DEA. The total number of elements in the model was targeted not to exceed 500,000 elements. The majority of elements (320,000 shell elements) were used to represent the DEA blocks and skid gear. In general, the fuselage model is primarily composed of shell elements representing airframe skins, ribs and stiffeners. Ballast representing rotor mass, tail mass, and fuel is incorporated in the FEM as concentrated mass elements. The lifting and pullback fixtures, that were added to the airframe for the impact test, were simulated as rigid shells. The platform that supports the data acquisition system (DAS) was mounted in the tail and was also modeled as a rigid shell. Material properties for the fuselage are based on the MD-500 Structural Repair Manual [21], which indicates that the fuselage material is primarily Aluminum 2024-T3, and has elastic-plastic properties.
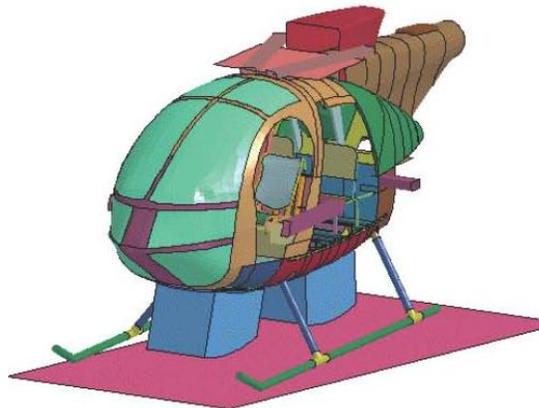
Figure 9. Model of the MD-500 Helicopter with DEA blocks.

In prior simulations, occupant models were included and the two DEA blocks were represented with shell elements [22-24]. To simplify the model, the occupants were removed and replaced using simple concentrated mass elements. In addition, the DEA shell elements were removed from the model and the DEA volume was discretized using solid elements. This change was made to enable evaluation of different material models assigned to solid elements representing the DEA in the MD-500 finite element model. In addition, it was anticipated that solid element DEA simulations would require less time to execute as compared with the shell-based DEA model. For the isotropic material models (Mat 63 and Mat 181), the two DEA blocks were included in one part definition. However, for the orthotropic material models (Mat 26 and Mat

142), each block was assigned its own part definition to account for different material directions due to the 20° cant angle of the front block.

Results of Simulating the Dynamic Crushing Response of Three DEA Components

Comparisons of the simulation predictions with the test data are made for each DEA component to evaluate the effectiveness of the four material models in predicting the DEA response. In each case, the predicted responses are filtered using an SAE CFC 180-Hz low-pass filter [18]. In addition, three correlation metrics were selected to assess the level of agreement between test and analysis for the DEA components. These metrics are initial peak acceleration; average crush stress, which is based on average acceleration that is calculated over the time interval of 0.0-0.03 seconds; and, peak acceleration during compaction.

Results for 59-Cell DEA

Test-analysis comparison plots are shown in Figure 10 with predictions from the isotropic material models (Mat 63 and Mat 181) shown in Figure 10(a) and predictions from the orthotropic material models (Mat 26 and Mat 142) shown in Figure 10(b). Note that for each material model, the average DEA response was used as the input load curve. Correlation metrics are provided in Table 6.

(a) Test with Mat 63 and Mat 181.   (b) Test data with Mat 26 and Mat 142.
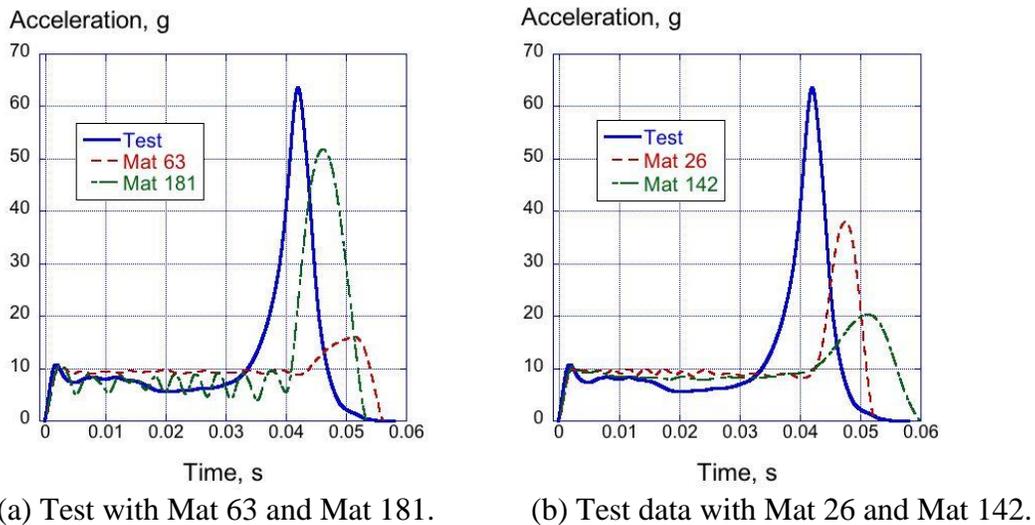
Figure 10. Test-analysis comparison plots for the 59-cell DEA component.

Table 6. Test-Analysis Correlation Metrics for the 59-Cell DEA Component Models.

Parameter	Test	Mat 63		Mat 181		Mat 26		Mat 142	
		Value	Error, %	Value	Error, %	Value	Error, %	Value	Error, %
Initial peak accel., g	10.8	10.4	3.7	10.6	1.9	9.7	10.2	10.2	5.6
Avg. crush stress, psi	16.8	20.8	-23.8	17.1	-1.8	20.7	-23.2	19.2	-14.3
Compaction peak, g	63.6	15.9	75.0	51.8	18.6	37.9	40.4	20.2	68.2

The results indicate that each material model was able to predict the initial peak acceleration within approximately 10% and the average crush stress within ±25%. However, predicted values of the peak compaction acceleration are off by as much as 75%. Of the four material models evaluated for the 59-cell DEA component, Mat 181 performed best among the three metrics considered, even though the predicted time of the peak compaction acceleration is delayed compared with the experiment.

Results for 104-Cell DEA

Test-analysis comparison plots are shown in Figure 11 for the 104-cell DEA component with predictions from the isotropic material models (Mat 63 and Mat 181) shown in Figure 11(a) and predictions from the orthotropic material models (Mat 26 and Mat 142) shown in Figure 11(b). Recall that for each material model, the average DEA response was used as the input load curve. Correlation metrics are provided in Table 7, with the exception of the peak compaction. This metric was removed since the test and analytic responses did not exhibit compaction.
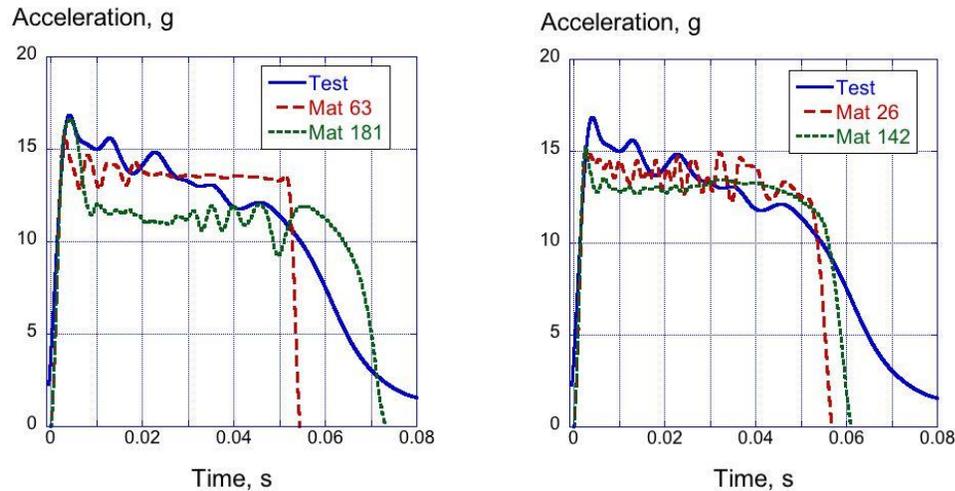
(a) Test with Mat 63 and Mat 181.   (b) Test data with Mat 26 and Mat 142.

Figure 11. Test-analysis comparison plots for the 104-cell DEA component.

For all material models, the level of agreement in predicting the initial acceleration and the sustained crushing stress is within 11% and 17%, respectively. In general, the analytical curves increased to an initial value between 15- to 17-g, then the acceleration level stayed fairly constant throughout the pulse. However, for Mat 181, the predicted response exhibited a sharp 5-g reduction in acceleration to approximately 12-g, following an initial peak of 16.7-g. Following the reduction, the acceleration level remained constant to the end of the pulse.

Table 7. Test-Analysis Correlation Metrics for the 104-Cell DEA Component Models.

Parameter	Test	Mat 63		Mat 181		Mat 26		Mat 142	
		Value	Error, %	Value	Error, %	Value	Error, %	Value	Error, %
Initial peak accel., g	16.9	15.8	6.5	16.7	1.2	15.1	10.7	15.2	7.7
Avg crush stress, psi	22.1	20.6	6.8	18.4	16.7	20.8	5.9	19.7	10.9

Results for 68-Cell DEA

Test-analysis comparison plots are shown in Figure 12 with predictions from the isotropic material models (Mat 63 and Mat 181) shown in Figure 12(a) and predictions from the orthotropic material models (Mat 26 and Mat 142) shown in Figure 12(b). Correlation metrics are provided in Table 8.

The results shown in Figure 12(a) indicate that the isotropic material models did a poor job of predicting the 68-cell canted DEA response. The Mat 63 curve failed to predict compaction, while the Mat 181 curve exhibited a compaction peak that was too high in magnitude by 58.2% and delayed in timing from the experimental peak. In comparison, the orthotropic models (Mat 26 and Mat 142) predicted the average crush stress within ±10% and the compaction peak within 30%. Overall, Mat 26 showed the best comparison with test.
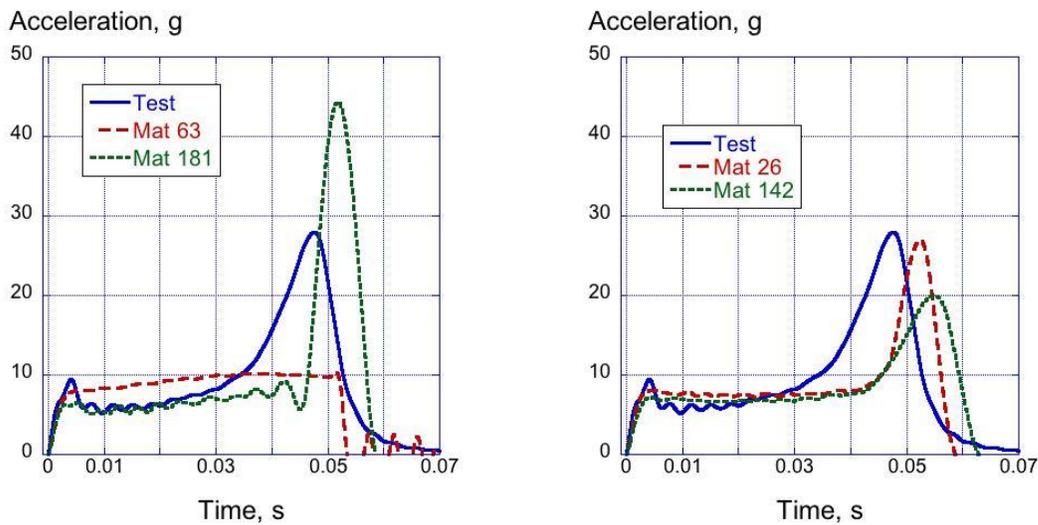
(a) Test with Mat 63 and Mat 181.   (b) Test data with Mat 26 and Mat 142.

Figure 12. Test-analysis comparison plots for the 68-cell canted DEA component.

Table 8. Test-Analysis Correlation Metrics for the 68-Cell DEA Component Models.

Parameter	Test	Mat 63		Mat 181		Mat 26		Mat 142	
		Value	Error, %	Value	Error, %	Value	Error, %	Value	Error, %
Initial peak accel., g	9.4	8.0	14.9	6.3	32.9	8.1	13.8	7.2	23.4
Avg crush stress, psi	16.1	19.9	-23.6	14.5	9.9	17.6	-9.3	16.0	0.6
Compaction peak, g	28.0	10.3	63.2	44.3	-58.2	26.9	3.9	20.0	28.6

Results of Simulating the Full-Scale Crash Test of the Retrofitted MD-500 Helicopter

Two channels were selected for test-analysis comparisons: one channel was located near the pilot seat box and the second was located on the passenger floor near the rear bulkhead. Test-analysis

comparisons are shown in Figure 13 for the simulations executed using the two isotropic material models (Mat 63 and Mat 181). Likewise, test-analysis comparisons are shown in Figure 14 for the simulations executed with the two orthotropic material models (Mat 26 and Mat 142). For each material model, the input load curves were based on the average stress-strain response. All accelerations shown in Figures 13 and 14 are in the local vertical axis direction and were filtered using a Butterworth 60-Hz digital filter. Predicted and experimental accelerations are generally low in magnitude, below 20-g, which are well tolerated by human occupants. Also, for most cases, the test and analysis curves at the pilot seat box location were a better match than for the passenger floor.

(a) Pilot seat box location.   (b) Passenger floor location.
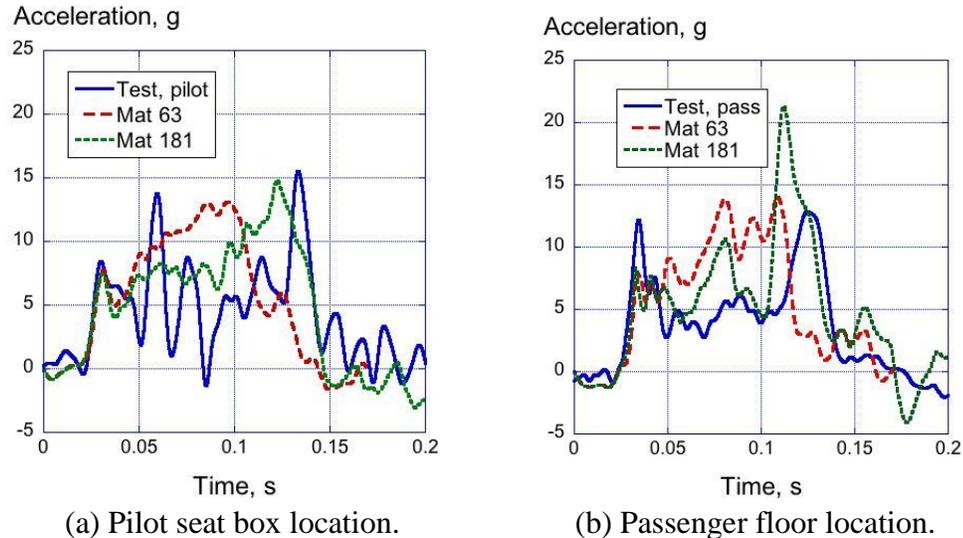
Figure 13. Test-analysis comparison plots for Mat 63 and Mat 181.

(a) Pilot seat box location.   (b) Passenger floor location.
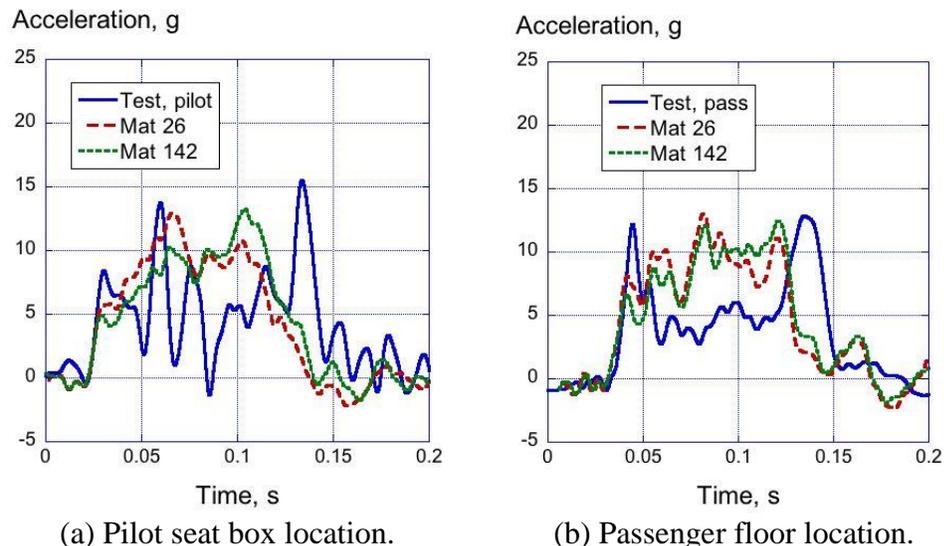
Figure 14. Test-analysis comparison plots for Mat 26 and Mat 142.

In addition to visual inspection of the plots, quantitative correlation metrics were evaluated using the Roadside Safety Verification and Validation Program (RSVVP) [17, 25], which is a software program that automatically assesses the similarities of two curves as part of the validation process of a numerical model. The program allows pre-processing of the two curves, including

filtering, phasing, and timing adjustments, etc. Sixteen different metrics are included that are classified into 3 categories: (1) magnitude-phase-comprehensive (MPC) metrics, (2) single-value metrics, and (3) analysis of variance (ANOVA) metrics.

For the MD-500 simulations, results are shown for the MPC metric developed by Sprague and Geers [26, 27], which provides a measure of the "goodness of fit" between two curves. Three parameters are calculated over a specified time interval: Sprague and Geers Magnitude (SGM), Sprague and Geers Phase (SGP), and Sprague and Geers Comprehensive (SGC), which is a combination of magnitude and phase. Generally, a value of less than 40 for SGM, SGP, or SGC is considered passing the criteria. Regarding the Sprague and Gears approach, it is important to note that the magnitude and phase metrics are independent of one another. For example, if changes are made to the magnitude of one curve, but the phase information remains the same, only the magnitude metric will change, and visa versa. It should also be noted that if two identical curves are being compared, all three metric values would be zero. Consequently, metric values close to zero are desired. As documented in References 17 and 27, sinusoidal pulses were compared using the Sprague and Geers approach within the RSVVP. One curve had the same phase as the "test" curve, but had a 20% higher magnitude. The resulting SGM value was 20, SGP was 0, and SGC was 20. Similarly, two sinusoidal curves of the same magnitude were evaluated in which one curve lagged the other in phase by -20%. The resulting SGM value was 0.1, SGP was 19.5, and SGC was 19.5. These test cases are highlighted to provide context for the metric values obtained in the MD-500 test-analysis comparison.

Metric correlations for the MD-500 simulations are provided in Table 9. Pre-processing of the test and analysis data within the RSVVP included filtering using an SAE CFC 180 filter, adjusting the time interval such that test and analysis curves matched, and minimizing the residuals by shifting one curve in time with respect to the other curve. According to the RSVVP, all models passed the Sprague and Geers criteria.

Table 9. Correlation metrics determined by RSVVP.

Metric	Mat 63		Mat 181		Mat 26		Mat 142	
	Pilot	Passenger	Pilot	Passenger	Pilot	Passenger	Pilot	Passenger
SGM	18.8	28.9	19.2	36.5	10.7	20.9	11.5	20.9
SGP	23.6	26.1	18.2	15.0	24.5	20.7	22.6	19.1
SGC	30.1	38.3	26.4	39.5	26.8	29.5	25.4	28.3

Discussion of the Results

As stated previously, a major advantage of using solid elements to represent the DEA was reduced run time when compared with shell element based simulations. For the DEA multi-cell components, the execution times for the solid element models described in this paper ranged from 21- to 40-minutes, regardless of material model. Similar shell-element-based models, described in Reference 28, required up to 87-minutes, for a common termination time of 0.1-s. All simulations were executed using LS-DYNA® SMP version 971 with four processors on a workstation computer. The MD-500 simulation using solid element representations of the DEA required 11 hours and 36 minutes to run to completion, whereas a similar model with shell-element-based representations of the DEA [29] required approximately 192 hours. Even though the solid element representation of the DEA was not able to predict the deformation modes seen

in the tests, this modeling approach provides a quick and efficient method of conducting DEA design studies.

This paper presents detailed descriptions of four material models that were evaluated in solid element representations of the DEA. Specific input parameters for each model are provided in tables. Even though the results are not shown in this paper, multiple studies were performed to determine the influence of parameter changes on the model response. These studies were necessary because many of the input values were unknown and estimates had to be input. For the more complicated material models (Mat 26 and Mat 142), it would be helpful to have guidelines or sample problems to show how certain parameters are used to control the material response.

As mentioned previously, each of the four material models selected for evaluation required input of a stress versus volumetric strain curve to define the material behavior. The average 59- and 104-cell response, depicted in Figure 3, was used in the DEA simulations because this curve had an average uniform crush stress of 19.8-psi, which is close to the design goal of 20-psi. However, in some cases, better agreement was achieved when either the 59-cell or the 104-cell responses were used in place of the average response. For example, the 59-cell DEA component model was executed in which the 59-cell stress-strain curve was used as input to Mat 26. A comparison plot of the test data with predicted responses using Mat 26 in which input curves were based on the 59-cell and average responses is shown in Figure 15. The timing and magnitude of the compaction peak are best predicted by Mat 26 when the input load curves are based on the 59-cell stress-strain response.

A full-scale simulation of the MD-500 model was executed with Mat 181 assigned to the DEA in which the input stress-strain curve was changed to the 104-cell response, shown in Figure 3. The vertical acceleration results for the pilot seat box and passenger floor locations are shown in Figure 16. These results show much improved agreement with test data when compared to the results obtained using the average input curve, as shown in Figure 13. In addition, the RSVVP program was used and the following metrics were obtained. For the pilot seat box location, SGM=7, SGP=16.9, and SGC=18.3. For the passenger floor location, SGM=18.9, SGP=13.3, and SGC=23.1. These metric values are improved when compared to the data shown in Table 9 for Mat 181 using the average input.

Finally, two different approaches were used for quantitative assessment of models. For the DEA components, simple percentage error calculations were made for three parameters deemed important in assessing the energy absorption responses of the DEA including initial peak acceleration, uniform crushing stress, and peak compaction acceleration. These measures, along with visual inspection of the test-analysis curves, provided a reasonable quantitative approach to assess the level of agreement between test and simulation. A more complex approach was used for the MD-500 model assessment using the RSVVP, a verification/validation program, to compare magnitude, phase, and comprehensive metrics between experimental and analytical responses for two locations on the airframe. Even though 16 different metrics were available, the Sprague and Geers [26] approach was used in this paper, based on the recommendations listed in Reference 25. Unlike the simple percentage error approach used for the DEA components, the Sprague and Geers method provides an assessment of the contributions of differences in magnitude and phase to the overall level of agreement.
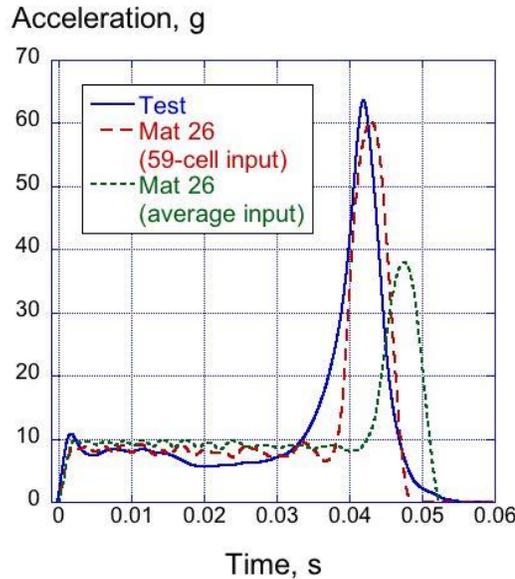
Figure 15. Test-analysis comparisons for the 59-cell DEA with Mat 26 in which the input load curves are varied.

(a) Pilot seat box comparison.   (b) Passenger floor comparison.
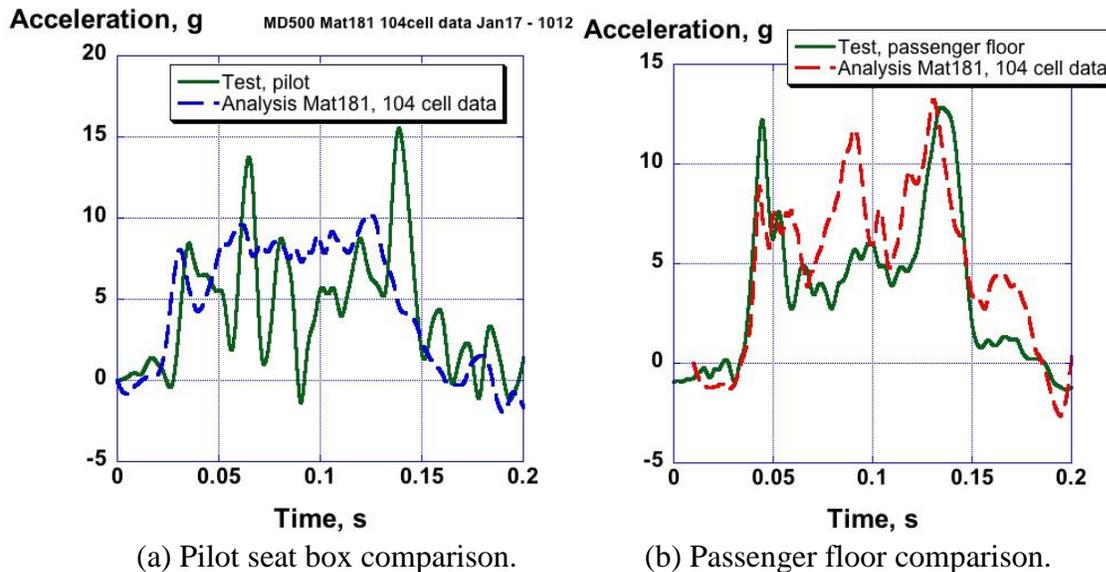
Figure 16. Test-analysis comparisons for the MD-500 model with Mat181 with 104 cell input.

Conclusions

This paper presents an evaluation of four different material models used in solid element representations of a composite deployable energy absorber (DEA). The models were executed to represent dynamic crush tests of multi-cell DEA components and a full-scale crash test of an MD-500 helicopter, retrofitted with two DEA blocks. All simulations were conducted using the nonlinear explicit transient dynamic code, LS-DYNA®. The four material models were: *MAT_CRUSHABLE_FOAM (Mat 63), *MAT_HONEYCOMB (Mat 26), *MAT_SIMPLI-FIED_RUBBER/FOAM (Mat 181), and *MAT_TRANSVERSELY_ANISOTROPIC_CRUSH-

ABLE_FOAM (Mat 142). Note that Mat 63 and Mat 181 are isotropic material models and Mat 26 and Mat 142 are transversely anisotropic material models.

Test-analysis correlation metrics were selected to assess the performance of each material model. For the case of the multi-cell DEA components, simple percentage error comparisons were made of initial peak acceleration, sustained crush stress, and compaction peak acceleration. For the 59-cell normal DEA component, Mat 181 showed the best comparison with test, predicting the initial acceleration and the uniform crush stress within 2%, and the compaction peak within 20%. For the 104-cell normal DEA, all four models were able to predict the initial peak acceleration within 11%; however, Mat 26 best predicted the uniform crushing response within 6%. The 104-cell DEA component did not achieve a compaction response, so no results were shown for that parameter. For the 68-cell off-axis DEA component, the two transversely anisotropic material models (Mat 26 and Mat 142) did the best job of predicting the test response.

For the full-scale crash of the MD-500 helicopter, test-analysis comparisons are shown at two locations: the pilot seat box and the passenger floor near the rear bulkhead. Magnitude-Phase-Comprehensive (MPC) correlation metrics developed by Sprague and Geers were assessed using the Roadside Safety Verification and Validation Program (RSVVP). All of the material models passed the correlation metrics with MPC values less than 40. Mat 26 had the lowest value of the magnitude metric (10.7), whereas Mat 181 had the lowest value of the phase metric (15.0), and Mat 142 had the lowest comprehensive value (25.4).

A major advantage of using solid elements to represent the DEA was reduced run time when compared with shell element based simulations. For the DEA component models, solid element models executed in 40-minutes or less, regardless of material model; whereas similar shell-element-based models required up to 87-minutes. These simulations were executed using LS-DYNA® Shared Memory Processor (SMP) version 971 with four processors on a Linux workstation computer. For the MD-500 finite element model using solid element representations of the DEA required approximately 12 hours, whereas a similar model with shell-element-based models of the DEA required 192 hours. Even though the solid element representation of the DEA was not able to predict the deformation modes seen in the tests, this modeling approach provides a quick and efficient method of conducting DEA design studies.

References

1. Jackson K.E., Fuchs Y.T., and Kellas S., "Overview of the NASA Subsonic Rotary Wing Aeronautics Research Program in Rotorcraft Crashworthiness," *Journal of Aerospace Engineering*, Special Issue on Ballistic Impact and Crashworthiness of Aerospace Structures, Volume 22, No. 3, July 2009, pp. 229-239.

2. Kellas S., "Deployable Rigid System for Crash Energy Management," US Patent Nos. 6,755,453 on June 29, 2004; 6,976,729 on December 20, 2005; and 7,040,658 on May 9, 2006.

3. Kellas S. and Jackson K.E., "Deployable System for Crash-Load Attenuation," *Journal of the American Helicopter Society*, Vol. 55, No. 4, October 2010, pp. 042001-1 through 042001-14.

4. Kellas S. and Jackson K.E., "Multi-Terrain Vertical Drop Tests of a Composite Fuselage Section," *Journal of the American Helicopter Society*, Vol. 55, No. 4, October 2010, pp. 042002-1 through 042002-042002-7.

5. Jackson K.E., Kellas S., Horta L.G., Annett M.S., Polanco M.A., Littell J.D., and Fasanella E.L., "Experimental and Analytical Evaluation of a Composite Honeycomb Deployable Energy Absorber," NASA Technical Memorandum, NASA-TM-2011-217301, November 2011.

6. Kellas S., Jackson K.E., and Littell J.D., "Full Scale Crash Test of a MD-500 Helicopter with Deployable Energy Absorbers," Proceedings of the 66th AHS Forum, Phoenix, AZ, May 11-13, 2010.

7. Littell J.D., Jackson K.E., and Kellas S., "Crash Test of an MD-500 Helicopter with a Deployable Energy Absorber Concept," Proceedings of the International Crashworthiness Conference, Leesburg, VA, September 22-24, 2010.

8. Littell J.D., "A Comparative Analysis of Two Full-Scale MD-500 Helicopter Crash Tests," Proceedings of the SEM 2011 Annual Conference, Uncasville, Connecticut, June 13 - 16, 2011.

9. Hallquist J.Q., "LS-DYNA Keyword User's Manual," Volumes I & II, Version 971, Livermore Software Technology Company, Livermore, CA, August, 2006.

10. Horta L.G., Jackson K.E., and Kellas S., "A Computational Approach for Model Update of an LS-DYNA Energy Absorbing Cell," *Journal of the American Helicopter Society*, Vol. 55, No. 3, July 2010, pp. 032011-1 – 032011-8.

11. Polanco M.A., Kellas S., and Jackson K.E., "Evaluation of Material Models within LS-DYNA for a Kevlar®/Epoxy Composite Honeycomb," Proceedings of the 65th AHS Forum, Grapevine, TX, May 27-29, 2009.

12. Polanco M.A., "Use of LS-DYNA to Assess Impact Response of a Shell-Based Kevlar/Epoxy Composite Honeycomb," Proceedings of the 11th LS-DYNA Users Conference, Dearborn, MI, June 6-8, 2010.

13. Jackson K.E., Kellas S., Annett M.S., Littell J., and Polanco M.A., "Evaluation of an Externally Deployable Energy Absorber for Crash Applications," Proceedings of the International Crashworthiness Conference, Leesburg, VA, September 22-24, 2010.

14. Fasanella E.L., Lyle K.H., and Jackson K.E., "Developing Soil Models for Dynamic Impact Simulations," Proceedings of the 65th AHS Forum, Grapevine, TX, May 27-29, 2009.

15. Jackson K. E. and Fuchs Y. T., "Comparison of ALE and SPH Simulations of Vertical Drop Tests of a Composite Fuselage Section into Water," Proceedings of the 10th International LS-DYNA Users Conference, Dearborn, MI, June 8-10, 2008.

16. Jackson K.E., "Predicting the Dynamic Crushing Response of a Composite Honeycomb Energy Absorber using a Solid-Element-Based Finite Element Model," Proceedings of the 11th International LS-DYNA Users Conference, Dearborn, MI, June 6-8, 2010.

17. Mongiardini M., Ray M.H., Anghileri M., "Development of a Software for the Comparison of Curves During the Verification and Validation of Numerical Models," Proceedings of the 7th European LS-DYNA Conference, Salzburg, Austria, May 14-15, 2009.

18. Society of Automotive Engineers, "Recommended Practice: Instrumentation for Impact Test - Part 1, Electronic Instrumentation," SAE J211/1, March 1995.

19. Roberts J., Merkle A., Biermann P., Ward E., Carkhuff B., Cain R., and O'Connor J., "Computational and Experimental Models of the Human Torso for Non-Penetrating Ballistic Impact," *J. Biomech*., 40 (1), 2007, pp. 125-136.

20. Hirth A., Du Bois P., Weimar K., "A Material Model for Transversely Anisotropic Crushable Foams in LS-DYNA," Proceedings of the 7th International LS-DYNA Users Conference, Dearborn, MI, May 19-21, 2002.

21. Anon, Structural Repair Manual, CSP–SRM–6, MD Helicopters, Inc, Mesa, AZ, May 2006.

22. Annett M. S., and Polanco M.A., "System-Integrated Finite Element Analysis of a Full-Scale Helicopter Crash Test with Deployable Energy Absorbers," Proceedings of the 66th AHS Forum, Phoenix, AZ, May 11-13, 2010.

23. Annett M. S., "LS-DYNA Analysis of a Full-Scale Helicopter Crash Test," Proceedings of the 11th International LS-DYNA Users Conference, Dearborn, MI, June 6-8, 2010.

24. Annett M.S. and Horta L. G., "Comparison of Test and Finite Element Analysis for Two Full-Scale Helicopter Crash Tests." 52nd AIAA/ASME/ASCE/AHS/ASC Structures, Structural Dynamics and Materials Conference, 4 - 7 April 2011, Denver, Colorado.

25. Marzougui D., Kan C-D., and Opiela K. S., "Comparison of the Crash Test and Simulation of an Angle Impact of a 2007 Chevrolet Silverado Pick-Up Truck into a New Jersey-Shaped Concrete Barrier for MASH Conditions," National Crash Analysis Center NACA 2010-W-001 Working Paper, July 2012.

26. Sprague M.A., and Geers T. L., "Spectral Elements and Field Separation for an Acoustic Fluid Subject to Cavitation," Journal of Computational Physics, Vol. 184, 2003, pp: 149-162.

27. Schwer L.E., "Validation Metrics for Response Histories: Perspectives and Case Studies." Engineering with Computers," Engineering with Computers (2007), 23:295-309.

28. Jackson K.E., Fasanella E. L., and Polanco M. A., "Simulating the Response of a Composite Honeycomb Energy Absorber: Part 1. Dynamic Crushing of DEA Components and Multi-Terrain Impacts," Proceedings of the 2012 ASCE Earth and Space Conference, Special Symposium on Ballistic Impact and Crashworthiness, to be held in Pasadena, CA on April 15-18, 2012.

29. Fasanella, E. L., Annett, M.S. and Polanco M. A., "Simulating the Response of a Composite Honeycomb Energy Absorber: Part 2. Full-Scale Impact Testing," Proceedings of the 2012 ASCE Earth and Space Conference, Special Symposium on Ballistic Impact and Crashworthiness, to be held in Pasadena, CA on April 15-18, 2012.